In Situ Atomic-Scale Observation of Reversible Potassium Storage in Sb_2S_3@Carbon Nanowire Anodes

Yong Cheng, Zhenpeng Yao, Qiaobao Zhang, Jiamin Chen, Weibin Ye, Shiyuan Zhou, Haodong Liu, and Ming-Sheng Wang**

Antimony trisulfide-based materials have drawn growing attention as promising anode candidates for potassium-ion batteries (PIBs) because of their high capacity and good working potential. Despite the extensive investigations on their electrochemical properties, the fundamental reaction mechanisms of Sb_2S_3 anodes, especially the reaction kinetics, structural changes, and phase evolutions, remain controversial or even largely unknown. Here, using in situ transmission electron microscopy, the entire potassiation–depotassiation cycles of carbon-coated Sb_2S_3 single-crystal nanowires are tracked in real time at the atomic scale. The potassiation of Sb_2S_3 involves multistep reactions including intercalation, conversion, and two-step alloying, and the final products are identified as cubic K_2S and hexagonal K_3Sb. These findings are confirmed by density functional theory calculations. Interestingly, a rocket-launching-like nanoparticle growth behavior is observed during alloying reactions, which is driven by the K^+ concentration gradient and release of stress. More impressively, the potassiated products (i.e., K_3Sb and K_2S) can transform into the original Sb_2S_3 phase during depotassiation, indicating a reversible phase transformation process, as distinct from other metal chalcogenide based electrodes. This work reveals the detailed potassiation/depotassiation mechanisms of Sb_2S_3-based anodes and can facilitate the analysis of the mechanisms of other metal chalcogenide anodes in PIBs.

1. Introduction

The rapidly growing markets of renewable energy grid storage and electric vehicles have created a strong demand for high-energy/power-density rechargeable batteries, such as lithium-ion batteries (LIBs).[1–9] Considering the increasing cost of lithium and the geographically uneven distribution of lithium resources, rechargeable batteries with cheap and abundant elements (e.g., sodium, potassium, magnesium, etc.) have attracted notable attention from the electrochemical energy storage field.[10–15] Among them, the potassium-ion batteries (PIBs) are one of the most competitive alternatives to LIBs.[16–18] Besides the abundant reserves and low cost, potassium possesses the second-lowest redox potential (K^+/K: −2.93 V, only slightly higher than Li (Li^+/Li: −3.03 V)) among all alkali and alkaline earth metals (Ca^{2+}/Ca: −2.87 V; Na^+/Na: −2.71 V; Mg^{2+}/Mg: −2.27 V), thus enabling PIBs to realize high working voltages. Despite these advantages, state-of-the-art PIBs currently suffer from several drawbacks, such as the inferior rate capability and unsatisfied cycling life. These problems can be attributed to the much larger ionic radius of K^+ (1.38 Å) compared with that of Li^+ (0.76 Å), which cause the drastic volume change in electrode materials and sluggish reaction kinetics through crystals.[19,20] To address these issues and design PIBs with enhanced electrochemical performances, searching for advanced electrode materials, which can accommodate the huge volume expansion and facilitate the K^+ diffusion, is highly required.

Antimony (Sb)-based materials, such as metallic Sb, alloys, oxides, chalcogenides, and their composites, have been intensively studied as the promising anodes for PIBs because of their large K^+ storage capacity, suitable working potential, and relatively low prices.[21] Among them, antimony trisulfide (Sb_2S_3) is of particular interest, as it delivers a higher

---

Y. Cheng, Prof. Q. Zhang, J. Chen, W. Ye, Prof. M.-S. Wang
State Key Lab of Physical Chemistry of Solid Surfaces
College of Materials
Xiamen University
Xiamen, Fujian 361005, China
E-mail: zhangqiaobao@xmu.edu.cn; mswang@xmu.edu.cn

Dr. Z. Yao
Department of Chemistry and Chemical Biology
Harvard University
12 Oxford Street, Cambridge, MA 02138, USA

The ORCID identification number(s) for the author(s) of this article can be found under https://doi.org/10.1002/adfm.202005417.

DOI: 10.1002/adfm.202005417

Dr. Z. Yao
Department of Chemistry and Department of Computer Science
University of Toronto
Toronto, Ontario M5S 3H6, Canada

S. Zhou
State Key Lab of Physical Chemistry of Solid Surfaces
Collaborative Innovation Center of Chemistry for Energy Materials
College of Chemistry and Chemical Engineering
Xiamen University
Xiamen, Fujian 361005, China

Dr. H. D. Liu
Department of Nanoengineering
University of California San Diego
La Jolla, CA 92093, USA

theoretical capacity than that of Sb anodes and exhibits enhanced electronic conductivity, mechanical stability, and better reaction reversibility compared with that of Sb-based oxides.[22,23] Recently, tremendous efforts have been devoted to the rational structure engineering and composite electrode design of Sb_2S_3-based anodes with improved K^+ storage.[24–27] However, the underlying mechanism of the enhanced performance of Sb_2S_3 electrodes has yet to be fully investigated. Although in situ/operando X-ray diffraction (XRD) has been conducted to observe the reaction processes of Sb_2S_3 during charging/discharging,[25,26] the detailed potassiation and depotassiation mechanisms remain controversial or largely unknown. In particular, the mechanisms on reaction kinetics, structural change and phase evolution need to be explored, which is critical for the development of novel Sb_2S_3-based anodes with a superior performance. To shed light on these issues, other in situ characterization techniques, such as in situ transmission electron microscopy (TEM),[28–35] are required to gain more detailed information.

In this work, the carbon-coated Sb_2S_3 single-crystal nanowires (Sb_2S_3@C) are adopted to systematically investigate their detailed electrochemical mechanisms during potassiation–depotassiation processes at the atomic scale by in situ TEM complemented with density functional theory (DFT) calculations. Three different types of reactions during potassiation are revealed, including intercalation ($Sb_2S_3 \rightarrow K_xSb_2S_3$), conversion ($K_xSb_2S_3 \rightarrow K_xS + Sb$), and alloying ($K_xS + Sb \rightarrow KSb + K_xS \rightarrow K_3Sb + K_2S$). The fully potassiated products, that is, K_3Sb and K_2S, are identified, and the latter phase has never been reported in previous researches.[25,26] Interestingly, a novel nanoparticle growth behavior resembling the launching of a rocket is observed during the alloying reaction, which can be ascribed to the K^+ concentration gradient and release of stress. Remarkably, unlike other metal chalcogenide based electrodes (e.g., SnS_2, FeS_2),[36,37] a reversible and symmetric phase transformation between the potassiated products and original Sb_2S_3 phase is revealed during depotassiation. To gain a more detailed understanding of the structural evolution during potassiation, DFT calculations are performed to predict the potassiated phases, which confirms our experimental observations. For the first time, these findings elucidate the full reaction nature of Sb_2S_3@C during potassiation/depotassiation and facilitate the mechanistic understanding of the electrochemical characteristics of other metal sulfides as electrode materials for PIBs.

2. Results and Discussion

2.1. Structural Characterization and Electrochemical Performance

Sb_2S_3@C nanowires were prepared via a facile hydrothermal method followed by carbonization (See Experimental Section for details, Supporting Information). The typical morphological and structural characteristics of Sb_2S_3@C nanowires are illustrated in **Figure 1**a–g. The XRD pattern of Sb_2S_3@C nanowires in Figure 1a shows sharp diffraction peaks that match well with the standard pattern of the orthorhombic Sb_2S_3 with a space group of Pbnm (PDF# 42-1393, $a = 11.239$ Å, $b = 11.313$ Å, $c = 3.841$ Å), indicating the high crystallinity and purity of Sb_2S_3. The scanning electron microscopy (SEM) image (Figure 1b) reveals that the Sb_2S_3@C nanowires have a diameter of 50–100 nm and a length of several micrometers. As revealed by the low-magnified TEM image in Figure 1c, a single Sb_2S_3@C nanowire typically consists of a Sb_2S_3 nanowire core fully coated with the 12 nm-thick amorphous carbon shell. According to the thermogravimetric analysis (TGA) results (Figure S1, Supporting Information), the carbon content of Sb_2S_3@C nanowires was calculated to be ≈13%. The selected area electron diffraction (SAED) pattern along the [100] zone axis (Figure 1d) confirms the single crystalline nature of the as-prepared Sb_2S_3 nanowires that grow preferentially along the [001] direction, consistent with previous reports.[38] Figure 1e shows the corresponding high-resolution TEM (HRTEM) image of the nanowire in Figure 1c, and the lattice fringe spacings of 5.67, 3.17, and 3.89 Å are indexed as (020), (021), and (001) planes of Sb_2S_3, respectively. The corresponding atomistic structure model is given in Figure 1f, where Sb_2S_3 consists of infinite chains of zigzag sheets of (Sb_4S_6) moieties along the *c*-axis.[39] EDS elemental mapping further visualizes the homogeneous distribution of S and Sb within the nanowire and C in the coating layer (Figure 1g).

The electrochemical performance of the Sb_2S_3@C anodes for PIBs were evaluated with the standard coin-type cell configuration. In galvanostatic discharge-charge profiles within 0.01–2.5 V at 0.05 A g^{-1} (Figure 1h), the first discharge and charge curves featured three and two potential plateaus, respectively, revealing the complicated multistep potassiation–depotassiation processes.[24] The corresponding first discharge and charge capacities were 1121 and 655 mAh g^{-1}, respectively, giving the first-cycle Coulombic efficiency (CE) of 58.4%. This low initial CE can be possibly attributed to irreversible reactions, electrolyte decomposition and inevitable formation of a solid electrolyte interface (SEI),[27] which can be mitigated by pre-potassiation treatment or optimization of the electrolyte.[40,41] The rate cycling performance of the Sb_2S_3@C electrode was better than that of the bare Sb_2S_3 electrode; that is, a reversible capacity of 163 mAh g^{-1} was delivered at 1 A g^{-1}, and the capacity of 548 mAh g^{-1} was still attained even as the current density was returned to 0.05 A g^{-1} (Figure 1i). In addition, as shown in Figure 1j, the Sb_2S_3@C electrode can maintain a reversible capacity of 293 mAh g^{-1} after 50 cycles, and this capacity was higher than that of the bare Sb_2S_3 electrode (72 mAh g^{-1} after 50 cycles). The dramatically improved performance of the Sb_2S_3@C electrode can be reasonably associated with the beneficial effect of the carbon coating because of its high electronic conductivity, high ionic conductivity, and good mechanical strength, which was thereafter verified by in situ TEM results.

2.2. Morphological Evolution during Potassiation–Depotassiation

To clarify the underlying reaction mechanisms of Sb_2S_3@C nanowires during potassiation–depotassiation process, a functioning solid-state K-Sb_2S_3@C nanobattery was constructed

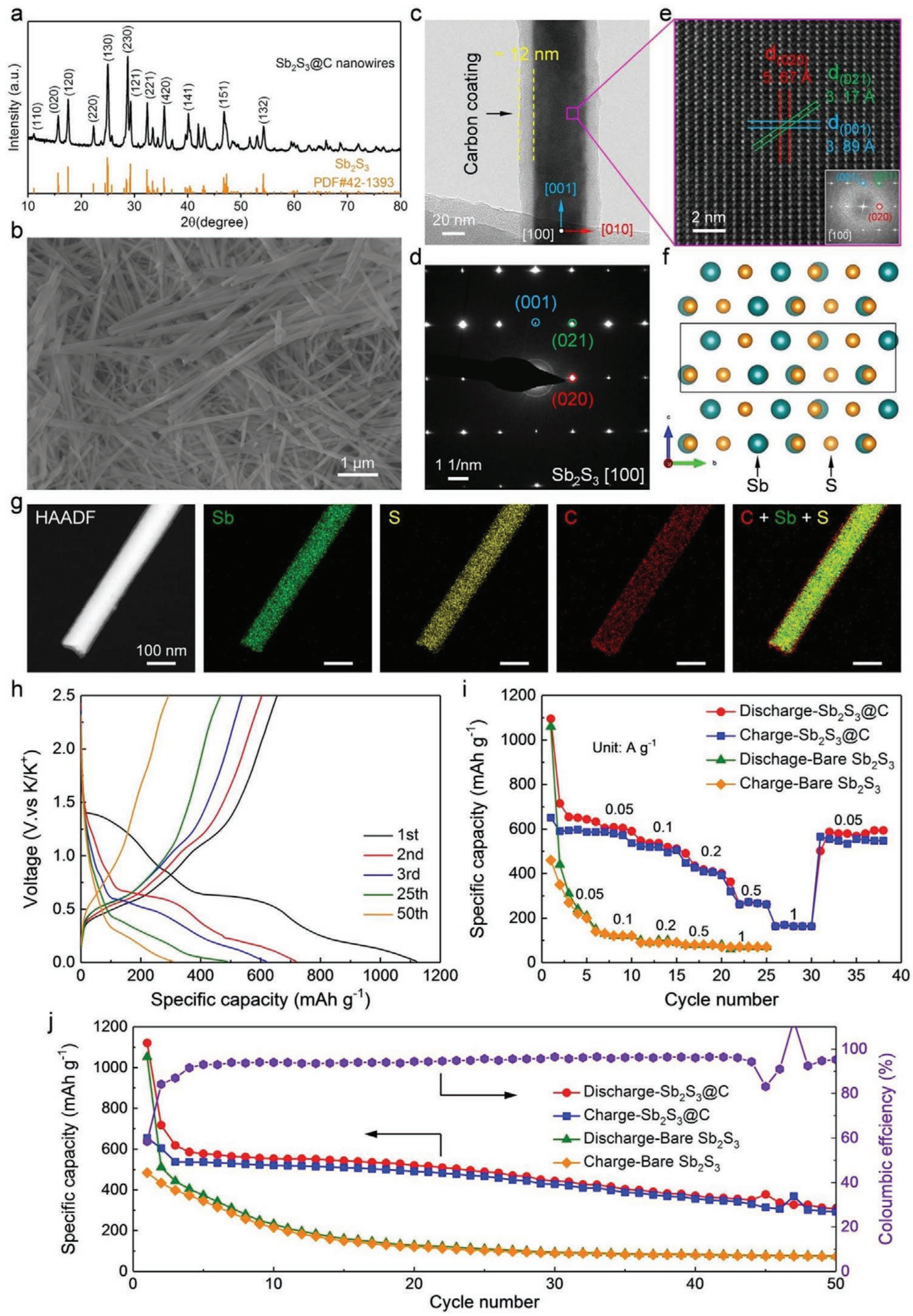

Figure 1. Structural characterization and electrochemical performance of Sb_2S_3@C nanowires. a) XRD pattern of Sb_2S_3@C nanowires and the standard diffraction pattern of Sb_2S_3. b) SEM image of Sb_2S_3@C nanowires. c) Low-magnified TEM image of a typical Sb_2S_3@C nanowire growing along the [001] direction. d–e) Corresponding SAED pattern and HRTEM image along [100] zone axis in (c). f) Atomic arrangement of the orthorhombic Sb_2S_3 crystal along [100] zone axis. g) EDS mapping images of a single Sb_2S_3@C nanowire. h) Galvanostatic charge/discharge curves of Sb_2S_3@C anodes cycled at 0.05 A g^{-1}. i) Rate performance of Sb_2S_3@C anodes at different current densities. e) Cycling performance and Coulombic efficiency of Sb_2S_3@C and bare Sb_2S_3 anodes at 0.05 A g^{-1}.

inside the TEM for in situ electrochemical tests. As schematically illustrated in **Figure 2**a, the nanobattery consists of a Sb_2S_3@C nanowire working electrode, a naturally grown K_2O solid electrolyte and a small piece of K metal as the counter electrode. The K_2O/K electrode mounted on the movable STM tungsten probe was driven to approach a nanowire. Once the contact between them was established, a bias of −3 V was applied on the nanowire to trigger the potassiation process. For depotassiation, instead, we switched the polarity of the applied bias with the voltage increased to +6 V. The real-time morphological evolution

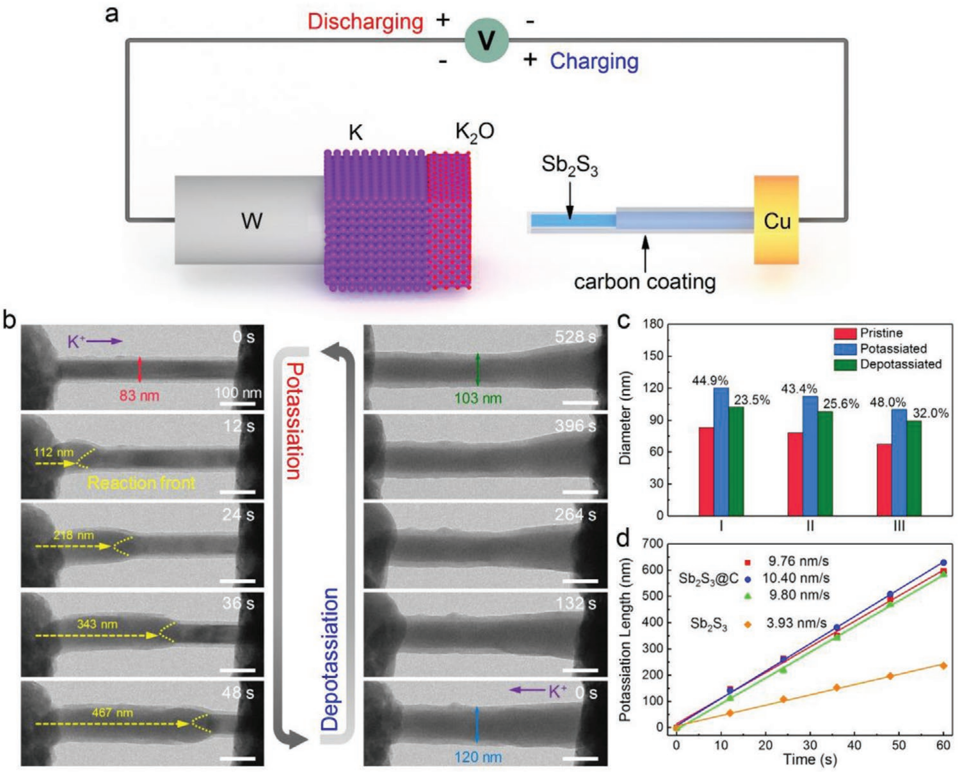

Figure 2. In situ observation of the morphological evolution of a single Sb_2S_3@C nanowire during potassiation–depotassiation cycling. a) Schematic illustration of the experimental setup for in situ electrochemical potassiation/depotassiation. b) Time-resolved in situ TEM images showing the volume expansion and contraction of nanowire during potassiation–depotassiation cycling. c) Diameter variation of three Sb_2S_3@C nanowires during potassiation–depotassiation cycling. d) Potassiation length plotted as a function of time for Sb_2S_3 and Sb_2S_3@C nanowires.

of a single Sb_2S_3@C nanowire during the first potassiation–depotassiation cycle is presented in Figure 2b (also see Movie S1 and S2, Supporting Information).

During potassiation, K^+ diffused from the contact side of the nanowire with the K_2O/K electrode and gradually propagated toward the other side, accompanied with the volume expansion and variation in contrast. A wedge-shaped reaction front (RF) was observed at the boundary between the potassiated and unpotassiated regions (marked with yellow dotted lines in Figure 2b). Similar to other in situ TEM experiments of lithiation/sodiation, the distinct wedge-shaped RF should be a result of the faster diffusion of K^+ along the surface of the nanowire than in the bulk.[42] The RF migration speed was calculated to be ≈9.8 nm s^{-1}, which can be comparable to that of some Na-ion battery systems, including Na-FeS_2 (6–11 nm s^{-1}) and Na-MoS_2 (≈3–7 nm s^{-1}).[37,43] This indicates that the potassiation kinetics of Sb_2S_3@C is relatively efficient, in spite of larger K^+ radius and mass than those of Na^+. After full potassiation, no apparent cracking or fracturing was observed although the diameter of the Sb_2S_3@C nanowire increased from 83 nm to 120 nm (≈45% expansion), suggesting the reliable mechanical stability of Sb_2S_3@C nanowires. This observation is in stark contrast to the bare Sb_2S_3 nanowire that had a larger diameter expansion (≈62%) and easily broke during potassiation (Figure S2, Supporting Information). Meanwhile, the Sb_2S_3@C nanowire did not undergo bending deformation during potassiation,[44] indicating an anisotropic expansion that was remarkable along the [010] direction but negligibly in the axial [001] direction. This finding is attributed to the relatively large interfacial spacing (5.67 Å) in the [010] direction that is more favorable for K^+ intercalation. Furthermore, we also selected a Sb_2S_3@C nanowire with its full length in the view of field to accurately estimate its volume expansion during potassiation (Figure S3, Supporting Information), and its diameter and length increased by ≈42% and ≈5% after potassiation, respectively. Thus, the corresponding overall volume expansion of Sb_2S_3@C is ≈111%, which is lower than that of other types of potassiation, such as the Sn-K alloying reaction (≈197%).[45] The relatively small volume expansion of Sb_2S_3@C may be caused by two possible factors. First, the K_xS matrix yielded by the additional conversion reaction can efficiently disperse and spatially confine the converted metal nanoparticles and offer a buffer to relax the stress induced by the subsequent alloying;[46] as such, the degree of the volume expansion of metal sulfide electrodes is usually smaller than that of the corresponding pure metal electrodes. Second, the carbon coating layer on the surface of Sb_2S_3 helps restrain radial expansion to further reduce the volume expansion.[44] Obviously, the small volume expansion can efficiently prevent the pulverization of electrodes and the loss of electrical contact, thereby enhancing the cyclic and rate performance of the Sb_2S_3@C electrode (as seen in Figure 1i–j).

During depotassiation, the electrode gradually shrank and still maintained its structural integrity upon the extraction of K^+ (Figure 2b), demonstrating the good reversibility and mechanical stability of Sb_2S_3@C. It should be noted that the final diameter of Sb_2S_3@C (103 nm, at 528 s) was still larger than that of the initial state (83 nm), which indicates that K^+ cannot completely return to the K_2O/K electrode, leading to the irreversible capacity loss in the first cycle (Figure 1h).

To minimize the beam effect, the above in situ experiments were also repeated under STEM-HAADF (i.e., scanning TEM-high angle annular dark field) imaging mode (Figure S4, Supporting Information). It further confirms the TEM imaging observation: the diameter of Sb_2S_3@C increases first and then decreases during the insertion and extraction of K^+, and no cracking or fracturing occurs. To exclude the influence of beam effect on the potassiation–depotassiation process of a Sb_2S_3@C nanowire, the beam-blank experiment was further conducted. As shown in Figure S5 (Supporting Information), similar results on morphology changes and phase evolution (as discussed below) can be observed. This confirms that the beam effect on the potassiation/depotassiation behaviors of Sb_2S_3@C is minor and can be neglected.

Through the repeated experiments, the average radial expansion and shrinkage ratio upon potassiation/depotassiation were found to be ≈45% and ≈27%, respectively (Figure 2c). By plotting the relationship between the propagating distance of the RF (L) and diffusion time (t), the K^+ transport kinetics in Sb_2S_3@C electrodes was also identified. As shown in Figure 2d, all the curves approximately follow a linear relationship ($L \propto t$), indicating that the potassiation of Sb_2S_3@C proceeds uniformly with a relatively fast RF migration speed of 9–10 nm s^{-1}. Notably, $L \propto t$ relationship indicates that K^+ diffusion in Sb_2S_3@C should be governed by a short-range interface reaction instead of a diffusion constrained long-range reaction, which follows $L \propto t^{1/2}$ relationship.[47] Additionally, carbon coating can significantly speed up the RF propagation by about 2.5 times because of the enhanced electronic conductivity.

2.3. Phase Evolution during Potassiation–Depotassiation

Next, the phase evolution of Sb_2S_3@C electrode during potassiation was investigated by using in situ SAED, and the main results are given in **Figure 3**a–d (Movie S3, Supporting Information). To reveal the whole phase evolution during potassiation more efficiently, a bunch of Sb_2S_3@C nanowires were selected to enhance the intensity of the obtained diffraction pattern when performing the in situ SAED experiment. Therefore, the time-resolved SAED patterns and the corresponding radially integrated intensity profiles (Figure 3a,c) show a polycrystalline-like structure of this bunch of Sb_2S_3@C nanowires at the initial state (0 s). After K^+ insertion (45 s), most of the diffraction spots of the pristine Sb_2S_3@C disappeared, and the (012) diffraction rings associated with Sb (PDF# 35-0732) and the diffuse intensity of amorphous phase emerge. These results suggest that a conversion reaction occurs immediately after K^+ intercalation into Sb_2S_3@C, consistent with the previous in situ XRD studies on Sb_2S_3 potassiation.[25] As the potassiation continued (185 s), the diffraction rings from Sb vanished, while four new diffraction rings appeared. They can be indexed as the $(11\bar{4})$, (211), (122), and (212) planes of KSb (PDF# 42-0791) as the intermediate phase due to the alloying between Sb and K. After full potassiation (376 s), KSb eventually transformed into the K_3Sb phase (PDF# 04-0643), as confirmed by the formation of the corresponding (201) and (112) diffraction rings. Apart from the diffraction rings of K_3Sb, five sharp diffraction rings, indexed as (200), (210), (211), (220), and (310) planes of K_2S (PDF# 23-0496), were detected in the final pattern. As a result, the fully potassiated products of Sb_2S_3@C are K_3Sb and K_2S, which is significantly different from the previous results (i.e., K_3Sb and K_2S_3; K_3Sb and K_2S_4).[25,26] Theoretically, the K_2S has the lowest formation energy in the K-S binary phase diagram.[48] But in some cases, K may react with S to form a thermodynamically unstable phase, namely, K_2S_2, and then, the K_2S_2 will transform into the K_2S_3 and K_2S phases via a disproportionation reaction ($2K_2S_2 \rightarrow K_2S_3 + K_2S$).[49] This is probably why K_2S_3 was reported in previous literatures.[25] However, in our case, owning to the small size of nanowires, Sb_2S_3 could be completely potassiated, resulting in the formation of the most stable K_2S phase. This phase can be further confirmed by the SAED pattern of a Sb_2S_3@C nanowire after prolonged potassiation, in which all diffraction rings can be assigned to K_2S and K_3Sb, not K_2S_3 (Figure S6, Supporting Information). These results also agree well with our theoretical calculation part. Besides, the K_3Sb in our case is a hexagonal phase,[27] rather than a cubic one.[25,26] Hence, the theoretical K^+ capacity of Sb_2S_3 can reach 946 mA h g^{-1}, which is about 3.4 times that of a graphite anode (279 mA h g^{-1}).[50]

It should also be pointed out that the diffraction patterns of K_3Sb and K_2S in Figure 3a were relatively diffuse with low intensities. This could be attributed to the incomplete K-Sb and K-S alloying reactions, which results in the formation of numerous amorphous phases, that is, K_xS and K_xSb,[46] as evidenced by the in situ HRTEM analyses below. Therefore, only a small amount of crystalline phases were detected, which can account for the low intensities of crystalline phases during depotassiation (as discussed below). To further confirm the final potassiated products, a Sb_2S_3@C nanowire was potassiated for a prolonged time. Figure S6 (Supporting Information) shows the corresponding diffraction pattern of the fully potassiated phases, where the diffraction rings were clear with high intensities, and can be reliably assigned to be crystalline K_3Sb and K_2S.

To better visualize the overall phase transformation of Sb_2S_3@C during potassiation, the radially integrated intensity profile (represented with false colors) as a function of time is further plotted (Figure 3b), which allows for quantitive analysis of the intensity evolutions of the (221)Sb_2S_3, (012)Sb, $(11\bar{4})$KSb, (210)K_2S, and (112)K_3Sb diffractions (Figure 3d). According to Figure 3b,d, the potassiation of Sb_2S_3@C can be divided into three stages: intercalation and conversion (0–75 s, Stage 1), alloying-I (75–210 s, Stage 2), and alloying-II (210 s to final, Stage 3). First, at Stage 1, the diffraction intensity associated with Sb_2S_3 gradually weakened, and the (012) diffraction of Sb emerged simultaneously. These results indicate that the subsequent conversion reaction occurs quickly, leading to the coexistence with the intercalation reaction. The corresponding reactions follow $Sb_2S_3 + xK^+ + xe^- \rightarrow K_xSb_2S_3 \rightarrow 2Sb + 3K_xS$. The fast conversion should be due to the large radius of K^+ that easily destroy the lattice of Sb_2S_3 in a very short time. Second, at Stage 2, all the diffraction intensity of pristine Sb_2S_3 and Sb

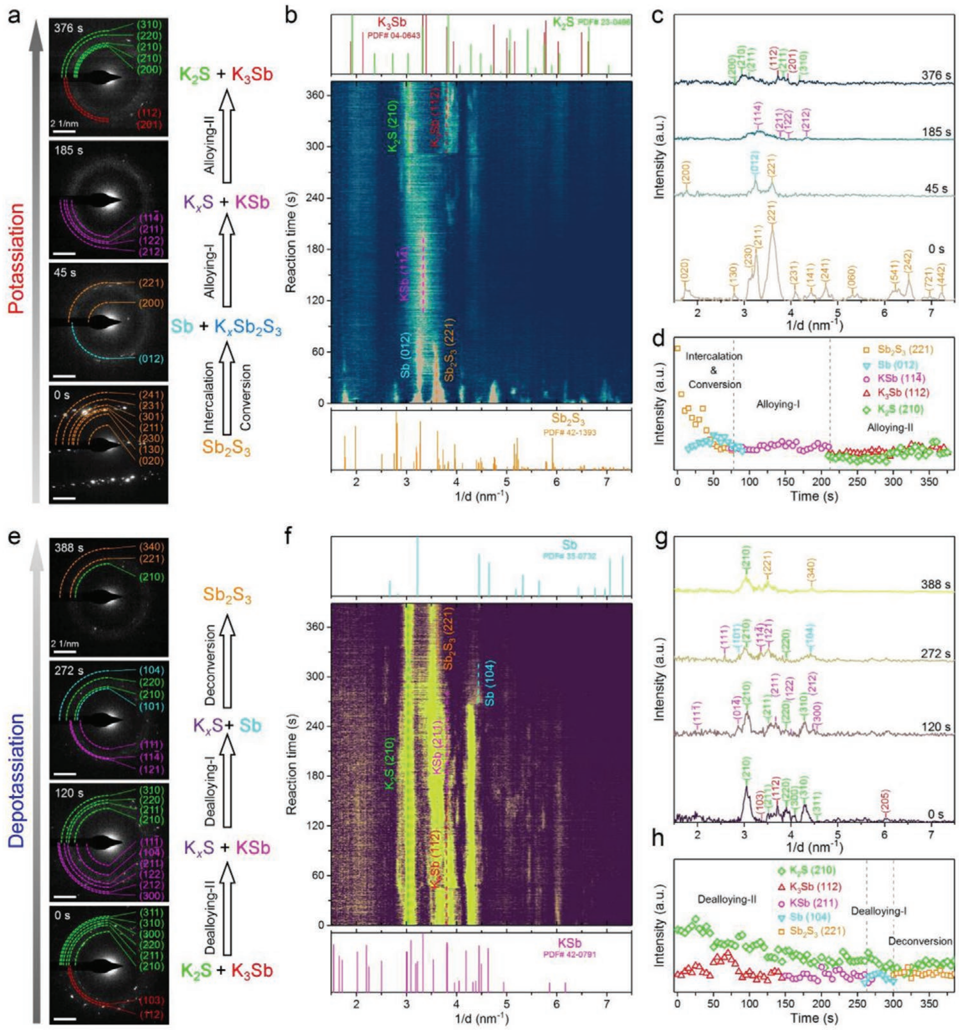

Figure 3. In situ SAED analysis of phase evolution for Sb_2S_3@C nanowires during potassiation–depotassiation cycling. a–d) Time-resolved SAED patterns, electron diffraction intensity profile as a function of reaction time, corresponding radial intensity profiles for time-resolved SAED patterns, intensity profiles for Sb_2S_3 (221), Sb (012), KSb (11$\bar{4}$), K_3Sb (112), K_2S (210) during potassiation. e–h) Time-resolved SAED patterns, electron diffraction intensity profile as a function of reaction time, corresponding radial intensity profiles for time-resolved SAED patterns, intensity profiles for Sb_2S_3 (221), Sb (104), KSb (211), K_3Sb (112), K_2S (210) during depotassiation.

disappeared because the excess K^+ intercalation triggered the K-Sb alloying reaction. The converted Sb reacted with K, initially forming KSb as an intermediate phase (i.e., Sb + K^+ + e^- → KSb). Finally, at Stage 3, the intermediate KSb continued to alloy with K to form K_3Sb, companied with the emergence of K_2S (i.e., $K_xS + KSb + (4\text{-}x)K^+ + (4\text{-}x)e^- \rightarrow K_2S + K_3Sb$). In short, the above results demonstrate that our Sb_2S_3@C underwent an intercalation and a conversion followed by a two-step alloying reactions during potassiation.

Another fully potassiated Sb_2S_3@C electrode was further selected, and a reversed bias was applied to initiate depotassiation and investigated the electrochemical phase transformations via in situ SAED. Figure 3e,g shows the representative time-resolved SAED patterns from Movie S4, Supporting Information, and the corresponding radially integrated intensity profiles, respectively. It is seen that the diffraction rings of K_3Sb gradually disappeared with depotassiation time, and the distinct diffraction rings from KSb (120 s) and Sb (272 s) appeared successively. Consistent with the in situ XRD results, our SAED findings reveal the reversible dealloying reaction (i.e., K_3Sb → KSb → Sb).[26] We also found that the diffraction ring of K_2S, another potassiated product, still existed although it was mostly decomposed. This indicates that K_2S is difficult to be completely converted during depotassiation, which accounts for the irreversible volume expansion in the morphological evolution as observed in Figure 2b. It is worth noting that the Sb formed after dealloying can further react with S (decomposed from K_2S) to regenerate Sb_2S_3 polycrystals, as evidenced by the reappearance of the diffraction rings of Sb_2S_3 in the final SAED pattern (388 s, Figure 3e,g). Figure 3f,h demonstrates that the depotassiation of Sb_2S_3@C also involves three stages: dealloying-II (0–275 s, stage 1), dealloying-I (275–300 s, stage 2), and deconversion (300–388 s, stage 3), the exact reversed process of its potassiation. The total depotassiation reaction of the three stages can be expressed as follows: $2K_3Sb + 3K_2S \rightarrow Sb_2S_3 + 12K^+ + e^-$. This result shows that the phase transformations in the entire conversion and alloying reaction between Sb_2S_3 and K are reversible. Additionally, no deintercalation occurs in Sb_2S_3@C nanowires because of the irreversible lattice destruction caused by K^+ insertion. Importantly, our observation on Sb_2S_3 regeneration offers solid evidence for the reversible deconversion process, which has never been reported in previous in situ XRD studies and other delithiation/desodiation of other metal chalcogenide based electrodes (e.g., SnS_2, FeS_2).[36,37]

2.4. Local Structure and Phase Evolution during Potassiation–Depotassiation

In addition to the in situ SAED investigation of the phase evolution, in situ HRTEM observation was also performed to clearly identify the local structural changes and corresponding phase evolution during potassiation–depotassiation cycling. As shown in **Figure 4**a$_1$, the pristine Sb_2S_3 nanowire core was highly crystalline, as evidenced by the magnified HRTEM image and the corresponding fast Fourier transform (FFT) pattern (Figure 4a$_2$). During K^+ insertion (Movie S5, Supporting Information), an interface with dark contrast emerged between the reacted and unreacted regions (Figure 4b$_1$). The magnified HRTEM image further indicates that the interface was associated with the formation of the potassium-intercalated $K_xSb_2S_3$ domain (≈5 nm, marked II in Figure 4b$_2$). This $K_xSb_2S_3$ domain is highlighted by two yellow borderlines (marked 1 and 2 in Figure 4b$_2$) that separate it from the pristine Sb_2S_3 (marked I in Figure 4b$_2$) and the conversion domain (marked III in Figure 4b$_2$), respectively. In the FFT pattern (inset in Figure 4b$_2$), the reflections became diffusive with slight splitting, indicating that a small amount of K^+ has been the inserted into the Sb_2S_3 lattice (forming $K_xSb_2S_3$) but not obviously changed its crystal structure. The

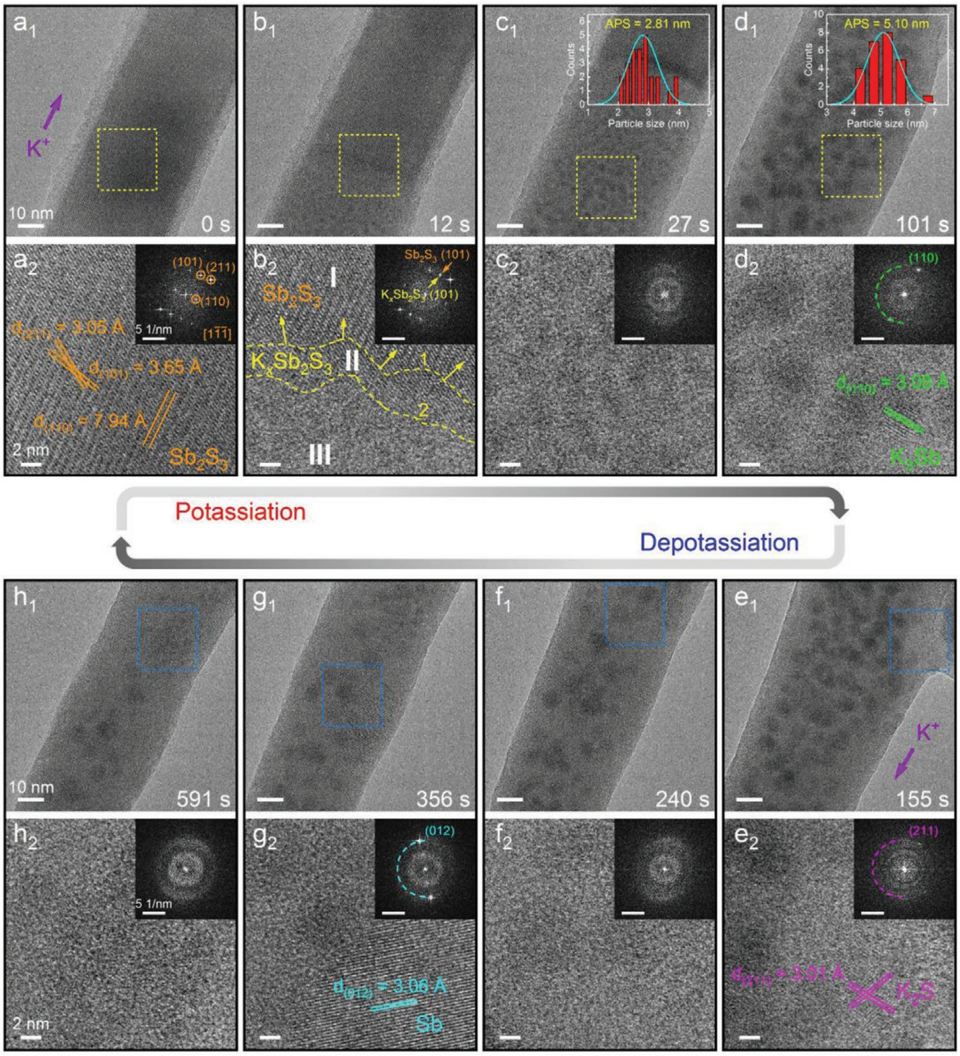

Figure 4. In situ HRTEM analysis of local structure and phase evolution for Sb_2S_3@C nanowires during potassiation–depotassiation cycling. a$_1$–d$_1$) Time-resolved HRTEM images and a$_2$–d$_2$) corresponding magnified regions with FFT patterns during potassiation. Insets in (c$_1$) and (d$_1$) show the variation of average nanoparticle size (APS). e$_1$–h$_1$) Time-resolved HRTEM images and e$_2$–h$_2$) corresponding magnified regions with FFT patterns during depotassiation.

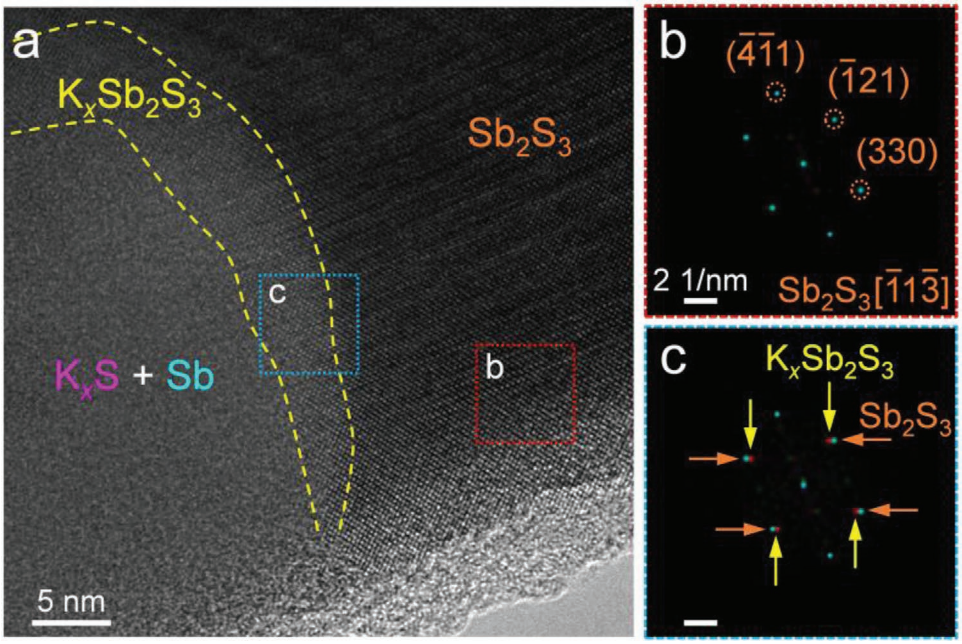

Figure 5. $K_xSb_2S_3$ domain in another Sb_2S_3@C nanowire during potassiation. a) The $K_xSb_2S_3$ domain separates the Sb_2S_3 and K_xS+Sb domains with two obvious borderlines. b,c) Corresponding FFT patterns in (a). The split of reflections is due to the insertion of K^+, indicating an increase of lattice spacing.

limited insertion of K^+ can be ascribed to the large K^+ radius, thus leading to the formation of a narrow $K_xSb_2S_3$ domain. **Figure 5**a shows another case where the $K_xSb_2S_3$ domain is more distinct from the pristine and converted regions during potassiation. From the corresponding FFT patterns of the two boxed regions in the HRTEM image (Figure 5b,c), one can see clearly that the reflections of (330) and ($\bar{1}21$) split into two spots, indicating that the pristine Sb_2S_3 phase has been partly transformed into $K_xSb_2S_3$ due to the K^+ insertion.

In domain III (Figure $4b_2$), the disappearance of the lattice fringes indicates the decomposition of $K_xSb_2S_3$ phase (also see Figure S7, Supporting Information). Meanwhile, a large number of tiny nanoparticles with dark contrast appeared in the amorphous matrix, similar to those observed in the in situ TEM studies on other conversion-type anodes.[51–53] Thus, it can be naturally deduced that these tiny nanoparticles were the converted Sb metal nanoparticles from the $K_xSb_2S_3$ phase. Due to the extremely small size, no reflection of Sb was detected in the FFT pattern (inset in Figure $4b_2$). As potassiation continued, the interface moved forward, whereas the as-generated small nanoparticles moved in the opposite directions and enlarged in size up to ≈5 nm with darker contrast (see the particle size distributions in Figure $4c_1$,d_1). This process visually resembles the launching of a rocket: its main body ($K_xSb_2S_3$ domain) is flying upward with the downward flame jetting (nanoparticles) (also see Figure S7 and Movie S6, Supporting Information). To the best of our knowledge, this phenomenon has never been observed before. Unlike the previous reports where the nanoparticles grow at stationary sites,[54–56] the nanoparticles in our case can move along for dozens of nanometers during their growth. This rocket-launching-like growth of nanoparticles can be associated with the formation of the K-Sb alloying phase, that is, the K-Sb nanoparticles during alloying need a sufficient K source to grow, which drives them to migrate toward the region with high K^+ concentration. In addition, the release of stress from intercalation may provide an extra driving force for the particles to move out of the highly stressed region.

Eventually, the crystalline Sb_2S_3@C nanowire evolved into a 1D skeleton embedded with a large number of nanoparticles (Figure $4d_1$). The HRTEM image and the corresponding FFT pattern in Figure $4d_2$ shows the nanocrystals with the lattice spacing of 3.08 Å, indicating the formation of K_3Sb. In addition, the HRTEM image in Figure $4e_1$,e_2 illustrates the formation of K_2S domains in the amorphous K_xS matrix. Thus, the final potassiated products of Sb_2S_3@C were K_3Sb and K_2S, consistent with our in situ SAED results. These results are also confirmed by other in situ HRTEM experiments (see more examples in Figure S8, Supporting Information). Additionally, it is worth noting that we can only observe amorphous K_xSb nanoparticles (with darker contrast), but lattice-resolved imaging of the intermediate KSb crystals was not available, which could be attributed to their small size and fast K-Sb reaction speed (see Movie S5, Supporting Information). However, based on the analysis of our in situ SAED results and the previous in situ XRD reports,[25,26] we believe the KSb should actually exist during the formation of K_3Sb.

During depotassiation, the size of the alloyed K_xSb nanoparticles decreased, and some of them vanished, due to the dealloying reaction (Figure $4f_1$,f_2; Movie S7, Supporting Information). Meanwhile, it should be noted that Sb atoms from dealloying reactions can gather to form a single larger crystal (Figure $4g_1$,g_2), which matches the in situ SAED results. Strikingly, upon further depotassiation, the single Sb crystal also dissolved (Figure $4h_1$,h_2), which could be attributed to the reversible conversion reaction to form Sb_2S_3. No strong reflection from Sb_2S_3 was found during our observation, suggesting that the deconversion process occurs locally without forming large crystals.[36,57]

2.5. Potassiation Mechanisms and DFT Calculations

On the basis of in situ SAED and HRTEM analysis, the potassiation mechanism of Sb_2S_3 is proposed to occur in the following way (**Figure 6**a): K^+ is first inserted into the lattice of Sb_2S_3 to form a very narrow $K_xSb_2S_3$ domain. Due to the large ionic radius of K^+, $K_xSb_2S_3$ is rapidly decomposed by the excess K^+, and then transformed into ultrafine Sb nanoparticles within the K_xS matrix via the subsequent conversion reaction. The dark contrasts near the RF in the TEM image (Figure 6b) confirm the formation of the $K_xSb_2S_3$ domain and Sb nanoparticles. No diffraction rings of $K_xSb_2S_3$ and Sb are visible in the corresponding SAED pattern because of the small size (Figure 6c). As potassiation goes on, the newly formed ultrafine Sb reacts with K to form K-Sb alloying nanoparticles, which exhibits a rocket-launching-like growth behavior. This process involves the formation of an intermediate KSb phase and the final potassiated K_3Sb phase. The nanopariticles in the TEM image (Figure 6b) with contrast being darker from left to right also clearly demonstrates their different growth stages, and the diffraction rings shown in the SAED pattern (Figure 6e) reveal the formation of K_3Sb as the final K-Sb alloying products.

In order to gain more insight into the electrochemical potassiation process of Sb_2S_3, especially the intercalation process, the DFT calculations were further conducted on exploring both equilibrium and nonequilibrium potassiation pathways. Phase diagrams, which represent the thermodynamic phase equilibria of multicomponent systems, have been widely used to predict phase reactions.[58] We thus constructed the K-Sb-S phase diagram ($T = 0$ K) (Figure 6f; Figure S9a, Supporting Information) by calculating the lowest energy structure of all known compositions from the Inorganic Crystal Structure Database (ICSD)[59] and determining the corresponding elemental reference state.[60] The equilibrium reaction of K-Sb_2S_3 can then be inferred via exploring all the possible phase combinations along the tie-line between Sb_2S_3 and K. As shown in Figure 6f and Figure S9 (Supporting Information), the equilibrium potassiation of Sb_2S_3 potentially underwent a series of three-phase regions with the determined multistep reaction route (Figure S9a,b, Supporting Information). The equilibrium potassiation voltage profile was computed accordingly, which aligns with the experimental curve in the alloying periods ($x > 3$, $K_xSb_2S_3$; Figure S9c, Supporting Information). However, a voltage gap (≈0.8 V) was observed at the early potassiation stage, implying the possible existence of nonequilibrium phases with a small amount of K^+ inserted. Meanwhile, considering the large number of intermediate phases involved in the alloying step, which also exhibit remarkable structural differences, it is probable that several of these phases are skipped in real-life reactions because of the vast mass transport required. Therefore, we investigated the non-equilibrium potassiation process around the early stages using an in-house code (see Experimental Section, Supporting Information).[61,62] For the alloying stage, the exact phases were determined by comparing the TEM image patterns between predicted phases and experimental observations. The intercalation chemistry of Sb_2S_3 was first studied through locating all the interstitials of its structure using the Materials Interface (Mint).[63] Then, with these located insertion sites, the non-equilibrium intermediate phase can be searched by exploring the geometrically distinct K/vacancy

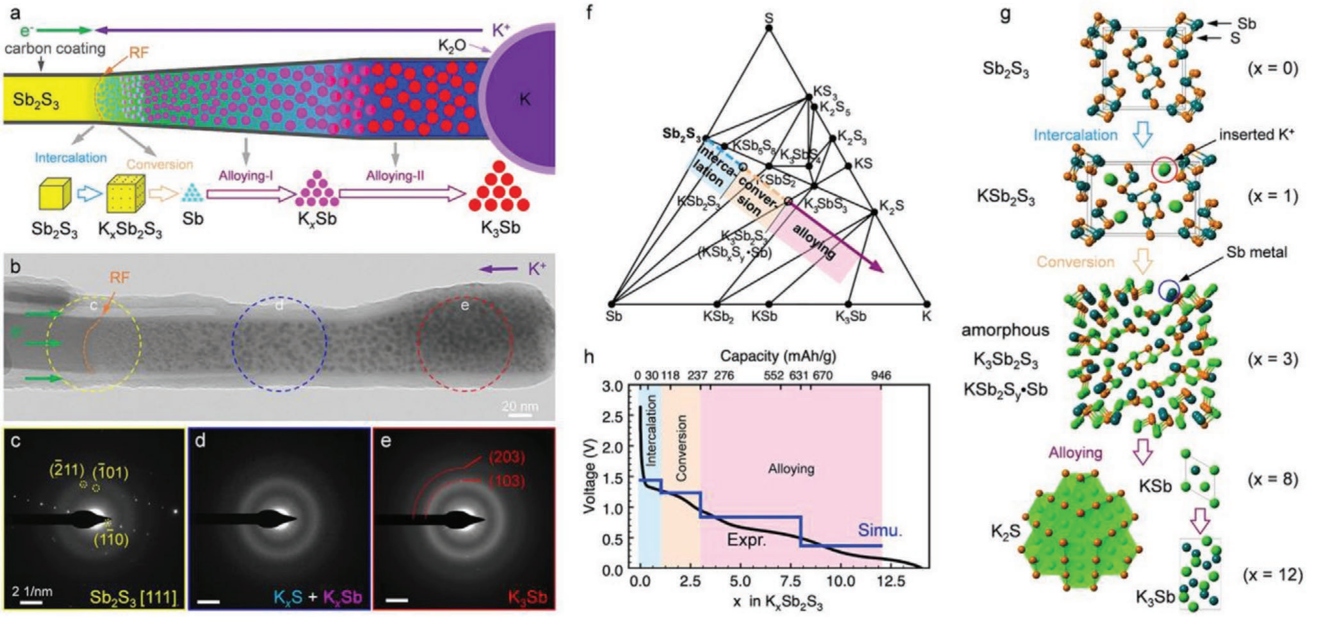

Figure 6. Reaction mechanism of the potassiation of Sb_2S_3 nanowire. a) Schematic drawing showing the rocket-launching-like nanoparticle growth along with phase evolution during potassiation process. b) TEM image showing the rocket-launching-like nanoparticle growth during potassiation process. c–e) Corresponding SAED in (b). f) K-Sb-S phase diagram from DFT calculations. g) Identified intermediate phases during potassiation process. h) Computed voltage profile using the intermediate phases versus the experimental voltage curve.

configurations on the as-identified stable insertion sites. Our results confirmed one nonequilibrium intermediate phase at $x = 1$ of $K_xSb_2S_3$, as shown in Figure S10 (Supporting Information). With the determined non-equilibrium and equilibrium phases during potassiation, the voltage profile was recalculated, which is in agreement with the experimental voltage curve (Figure 6h). Then the whole potassiation process is found to proceed as follows (see Figure 6g): i) Intercalation stage ($0 < x < 1$). K^+ occupies the interstitial sites, and considering the large ionic size of K^+, this period is speculated to be short, with huge lattice changes brought to the structure. ii) Conversion stage ($2 < x < 3$). Sb metal atoms start to be excluded from the structure, leading to the amorphization and loss of stability of the intercalated phase. iii) Two-step alloying stage ($3 < x < 12$). K_2S/KSb phases and K_2S/K_3Sb phases emerge successively. The evolution of the atomic structures revealed from DFT calculations verifies the HRTEM observations, as discussed in previous sections.

3. Conclusions

In summary, we apply in situ TEM combined with DFT calculations to comprehensively study the detailed morphological characteristics, phase evolutions, and the associated dynamic behavior of carbon-coated Sb_2S_3 nanowires in real-time potassiation–depotassiation processes. In situ low-magnified TEM observations show that the RF is governed by a short-range interface reaction during the insertion of K^+ into Sb_2S_3@C, and the average speed of RF migration is 9–10 nm s^{-1}, which is faster than that of bare Sb_2S_3 nanowires. Although the nanowires undergo volume expansion and contraction, they can maintain their structural integrity without pulverization and cracking, proving the good mechanical stability of Sb_2S_3@C electrodes. In situ SAED results demonstrate that Sb_2S_3@C experiences multistep reactions during potassiation, namely, intercalation, conversion and two-step alloying ($Sb_2S_3 \rightarrow K_xSb_2S_3 \rightarrow K_xS + Sb \rightarrow K_xS + KSb \rightarrow K_2S + K_3Sb$). The fully potassiated products are determined to be cubic K_2S and hexagonal K_3Sb, which are different from previous results of in situ/operando XRD. In particular, a reversible phase transformation from K_2S and K_3Sb to the original Sb_2S_3 phase is observed during depotassiation, distinct from other reports om metal chalcogenide based electrodes. In situ HRTEM results also demonstrate the reversible phase transformation at the atomic scale. Intriguingly, due to the K^+ concentration gradient and release of stress, the K-Sb alloying nanoparticles grow in a manner similar to the launching of a rocket. DFT calculations further validate our experimental results, and elucidate the detailed atomic structural evolutions during potassiation. These findings shed light on the fundamental understanding of the potassium ion storage mechanism of Sb_2S_3, and would be helpful to the development of high-performance PIBs.

Supporting Information

Supporting Information is available from the Wiley Online Library or from the author.

Acknowledgements

Y.C. and Z.Y. contributed equally to this work. This work was supported by the National Natural Science Foundation of China (Grant Nos. 21703185, 51872098, 61471307), the National Key R&D Program of China (Grant No. 2018YFB0905400), the Leading Project Foundation of Science Department of Fujian Province (Grant No. 2018H0034) and the "Double-First Class" Foundation of Materials and Intelligent Manufacturing Discipline of Xiamen University. Computations were performed on the Niagara supercomputer at the SciNet HPC Consortium. SciNet is funded by: the Canada Foundation for Innovation; the Government of Ontario; Ontario Research Fund-Research Excellence; and the University of Toronto.

Conflict of Interest

The authors declare no conflict of interest.

Keywords

antimony trisulfide, potassium-ion batteries, reversible phase transformations

Received: June 27, 2020
Revised: August 19, 2020

---

[1] B. Dunn, H. Kamath, J. M. Tarascon, *Science* **2011**, *334*, 928.
[2] D. Larcher, J. M. Tarascon, *Nat. Chem.* **2015**, *7*, 19.
[3] X. Y. Yue, X. L. Li, W. W. Wang, D. Chen, Q. Q. Qiu, Q. C. Wang, X. J. Wu, Z. W. Fu, Z. Shadike, X. Q. Yang, Y. N. Zhou, *Nano Energy* **2019**, *60*, 257.
[4] X. Y. Yue, W. W. Wang, Q. C. Wang, J. K. Meng, X. X. Wang, Y. Song, Z. W. Fu, X. J. Wu, Y. N. Zhou, *Energy Storage Mater.* **2019**, *21*, 180.
[5] D. Zhang, A. Dai, M. Wu, K. Shen, T. Xiao, G. Hou, J. Lu, Y. Tang, *ACS Energy Lett.* **2020**, *5*, 180.
[6] K. Shen, Z. Wang, Y. Ying, D. Zhang, C. Jin, X. Bi, G. Hou, H. Cao, L. Wu, G. Zheng, Y. Tang, X. Tao, J. Lu, *Adv. Energy Mater.* **2019**, *9*, 1900260.
[7] Q. Zhang, H. Chen, L. Luo, B. Zhao, H. Luo, X. Han, J. Wang, C. Wang, Y. Yang, T. Zhu, M. Liu, *Energy Environ. Sci.* **2018**, *11*, 669.
[8] Z. Zheng, P. Li, J. Huang, H. Liu, Y. Zao, Z. Hu, L. Zhang, H. Chen, M. S. Wang, D. L. Peng, Q. Zhang, *J. Energy Chem.* **2020**, *41*, 126.
[9] Z. Zheng, H. H. Wu, H. Liu, Q. Zhang, X. He, S. Yu, V. Petrova, J. Feng, R. Kostecki, P. Liu, D. L. Peng, M. Liu, M. S. Wang, *ACS Nano* **2020**, *14*, 9545.
[10] Y. Sun, N. Liu, Y. Cui, *Nat. Energy* **2016**, *1*, 16071.
[11] C. Vaalma, D. Buchholz, M. Weil, S. Passerini, *Nat. Rev. Mater.* **2018**, *3*, 18013.
[12] J. Y. Hwang, S. T. Myung, Y. K. Sun, *Adv. Funct. Mater.* **2018**, *28*, 1802938.
[13] H. D. Yoo, I. Shterenberg, Y. Gofer, G. Gershinsky, N. Pour, D. Aurbach, *Energy Environ. Sci.* **2013**, *6*, 2265.
[14] G. Fang, J. Zhou, A. Pan, S. Liang, *ACS Energy Lett.* **2018**, *3*, 2480.
[15] M. C. Lin, M. Gong, B. Lu, Y. Wu, D. Y. Wang, M. Guan, M. Angell, C. Chen, J. Yang, B. J. Hwang, H. Dai, *Nature* **2015**, *520*, 324.
[16] I. Sultana, M. M. Rahman, Y. Chen, A. M. Glushenkov, *Adv. Funct. Mater.* **2018**, *28*, 1703857.
[17] H. Kim, J. C. Kim, M. Bianchini, D. H. Seo, J. Rodriguez-Garcia, G. Ceder, *Adv. Energy Mater.* **2018**, *8*, 1702384.

[18] Y. Li, Q. Zhang, Y. Yuan, H. Liu, C. Yang, Z. Lin, J. Lu, *Adv. Energy Mater.* **2020**, *10*, 2000717.
[19] W. Zhang, Y. Liu, Z. Guo, *Sci. Adv.* **2019**, *5*, eaav7412.
[20] R. Rajagopalan, Y. Tang, X. Ji, C. Jia, H. Wang, *Adv. Funct. Mater.* **2020**, *30*, 1909486.
[21] H. Gao, X. Guo, S. Wang, F. Zhang, H. Liu, G. Wang, *EcoMat.* **2020**, *2*, e12027.
[22] Y. Denis, P. V. Prikhodchenko, C. W. Mason, S. K. Batabyal, J. Gun, S. Sladkevich, A. G. Medvedev, O. Lev, *Nat. Commun.* **2013**, *4*, 2922.
[23] X. Xiong, G. Wang, Y. Lin, Y. Wang, X. Ou, F. Zheng, C. Yang, J. H. Wang, M. Liu, *ACS Nano* **2016**, *10*, 10953.
[24] Y. Lu, J. Chen, *Sci. China Chem.* **2017**, *60*, 1533.
[25] Y. Liu, Z. Tai, J. Zhang, W. K. Pang, Q. Zhang, H. Feng, K. Konstantinov, Z. Guo, H. K. Liu, *Nat. Commun.* **2018**, *9*, 3645.
[26] J. Wang, L. Fan, Z. Liu, S. Chen, Q. Zhang, L. Wang, H. Yang, X. Yu, B. Lu, *ACS Nano* **2019**, *13*, 3703.
[27] L. Yang, W. Hong, Y. Tian, G. Zou, H. Hou, W. Sun, X. Ji, *Chem. Eng. J.* **2020**, *385*, 123838.
[28] J. Y. Huang, L. Zhong, C. M. Wang, J. P. Sullivan, W. Xu, L. Q. Zhang, S. X. Mao, N. S. Hudak, X. H. Liu, A. Subramanian, *Science* **2010**, *330*, 1515.
[29] Y. Yuan, K. Amine, J. Lu, R. Shahbazian-Yassar, *Nat. Commun.* **2017**, *8*, 15806.
[30] X. Lan, W. Ye, H. Zheng, Y. Cheng, Q. Zhang, D. L. Peng, M. S. Wang, *Nano Energy* **2019**, *66*, 104178.
[31] W. Ye, F. Pei, X. Lan, Y. Cheng, X. Fang, Q. Zhang, N. Zheng, D. L. Peng, M. S. Wang, *Adv. Energy Mater.* **2020**, *10*, 1902956.
[32] X. Li, L. Zhao, P. Li, Q. Zhang, M. S. Wang, *Nano Energy* **2017**, *42*, 122.
[33] Y. Chen, Z. Wang, X. Li, X. Yao, C. Wang, Y. Li, W. Xue, D. Yu, S. Y. Kim, F. Yang, A. Kushima, G. Zhang, H. Huang, N. Wu, Y. W. Mai, J. B. Goodenough, J. Li, *Nature* **2020**, *578*, 251.
[34] L. Zhang, T. Yang, C. Du, Q. Liu, Y. Tang, J. Zhao, B. Wang, T. Chen, Y. Sun, P. Jia, H. Li, L. Geng, J. Chen, H. Ye, Z. Wang, Y. Li, H. Sun, X. Li, Q. Dai, Y. Tang, Q. Peng, T. Shen, S. Zhang, T. Zhu, J. Huang, *Nat. Nanotechnol.* **2020**, *15*, 94.
[35] M. G. Boebinger, O. Yarema, M. Yarema, K. A. Unocic, R. R. Unocic, V. Wood, M. T. McDowell, *Nat. Nanotechnol.* **2020**, *15*, 475.
[36] S. Hwang, Z. Yao, L. Zhang, M. Fu, K. He, L. Mai, C. Wolverton, D. Su, *ACS Nano* **2018**, *12*, 3638.
[37] L. Yao, W. Xia, H. Zhang, H. Dong, H. L. Xin, P. Gao, R. Cai, C. Zhu, Y. Wu, M. Nie, *Nano Energy* **2019**, *60*, 424.
[38] Y. Zhao, A. Manthiram, *Chem. Commun.* **2015**, *51*, 13205.
[39] I. Efthimiopoulos, C. Buchan, Y. Wang, *Sci. Rep.* **2016**, *6*, 24246.
[40] J. Lu, C. Wang, H. Yu, S. Gong, G. Xia, P. Jiang, P. Xu, K. Yang, Q. Chen, *Adv. Funct. Mater.* **2019**, *29*, 1906126.
[41] Y. Wang, Z. Wang, Y. Chen, H. Zhang, M. Yousaf, H. Wu, M. Zou, A. Cao, R. P. S. Han, *Adv. Mater.* **2018**, *30*, 1802074.
[42] X. H. Liu, H. Zheng, L. Zhong, S. Huang, K. Karki, L. Q. Zhang, Y. Liu, A. Kushima, W. T. Liang, J. W. Wang, J. H. Cho, E. Epstein, S. A. Dayeh, S. T. Picraux, T. Zhu, J. Li, J. P. Sullivan, J. Cumings, C. Wang, S. X. Mao, Z. Z. Ye, S. Zhang, J. Y. Huang, *Nano Lett.* **2011**, *11*, 3312.
[43] P. Gao, L. Wang, Y. Zhang, Y. Huang, K. Liu, *ACS Nano* **2015**, *9*, 11296.
[44] L. Zhao, H. H. Wu, C. Yang, Q. Zhang, G. Zhong, Z. Zheng, H. Chen, J. Wang, K. He, B. Wang, T. Zhu, *ACS Nano* **2018**, *12*, 12597.
[45] Q. Wang, X. Zhao, C. Ni, H. Tian, J. Li, Z. Zhang, S. X. Mao, J. Wang, Y. Xu, *J. Phys. Chem. C* **2017**, *121*, 12652.
[46] K. Yin, M. Zhang, Z. D. Hood, J. Pan, Y. S. Meng, M. Chi, *Acc. Chem. Res.* **2017**, *50*, 1513.
[47] J. H. Park, Y. S. Choi, Y. W. Byeon, J. P. Ahn, J. C. Lee, *Nano Energy* **2019**, *65*, 104041.
[48] P. Xiong, X. Han, X. Zhao, P. Bai, Y. Liu, J. Sun, Y. Xu, *ACS Nano* **2019**, *13*, 2536.
[49] O. El Jaroudi, E. Picquenard, A. Demortier, J. Lelieur, J. Corset, *Inorg. Chem.* **2000**, *39*, 2593.
[50] Z. Jian, W. Luo, X. Ji, *J. Am. Chem. Soc.* **2015**, *137*, 11566.
[51] F. Wang, H. C. Yu, M. H. Chen, L. Wu, N. Pereira, K. Thornton, A. Van der Ven, Y. Zhu, G. G. Amatucci, J. Graetz, *Nat. Commun.* **2012**, *3*, 1201.
[52] M. G. Boebinger, D. Yeh, M. Xu, B. C. Miles, B. Wang, M. Papakyriakou, J. A. Lewis, N. P. Kondekar, F. J. Q. Cortes, S. Hwang, X. Sang, D. Su, R. R. Unocic, S. Xia, T. Zhu, M. T. McDowell, *Joule* **2018**, *2*, 1783.
[53] M. Fu, Z. Yao, X. Ma, H. Dong, K. Sun, S. Hwang, E. Hu, H. Gan, Y. Yao, E. A. Stach, C. Wolverton, D. Su, *Nano Energy* **2019**, *63*, 103882.
[54] M. Gu, Z. Wang, J. G. Connell, D. E. Perea, L. J. Lauhon, F. Gao, C. Wang, *ACS Nano* **2013**, *7*, 6303.
[55] Q. Gao, M. Gu, A. Nie, F. Mashayek, C. Wang, G. M. Odegard, R. Shahbazian-Yassar, *Chem. Mater.* **2014**, *26*, 1660.
[56] K. He, Z. Yao, S. Hwang, N. Li, K. Sun, H. Gan, Y. Du, H. Zhang, C. Wolverton, D. Su, *Nano Lett.* **2017**, *17*, 5726.
[57] S. Kim, Z. Yao, J. M. Lim, M. C. Hersam, C. Wolverton, V. P. Dravid, K. He, *Adv. Mater.* **2018**, *30*, 1804925.
[58] A. R. Akbarzadeh, V. Ozoliņš, C. Wolverton, *Adv. Mater.* **2007**, *19*, 3233.
[59] A. Belsky, M. Hellenbrandt, V. L. Karen, P. Luksch, *Acta Crystallogr., Sect. B: Struct. Crystallogr. Cryst. Chem.* **2002**, *58*, 364.
[60] Z. Yao, V. I. Hegde, A. Aspuru-Guzik, C. Wolverton, *Adv. Energy Mater.* **2019**, *9*, 1802994.
[61] Z. Yao, S. Kim, J. He, V. I. Hegde, C. Wolverton, *Sci. Adv.* **2018**, *4*, eaao6754.
[62] Z. Yao, S. Kim, M. Aykol, Q. Li, J. Wu, J. He, C. Wolverton, *Chem. Mater.* **2017**, *29*, 9011.
[63] L. Ward, K. Michel, Materials/mint: Initial release, https://doi.org/10.5281/zenodo.167890 (accessed: November 2016).